Numerical investigation of infragravity wave amplifications during harbor oscillations influenced by variable offshore topography

Gao, Junliang
School of Naval Architecture and Ocean Engineering, Jiangsu University of Science and Technology

Ji, Chunyan
School of Naval Architecture and Ocean Engineering, Jiangsu University of Science and Technology

Ma, Xiaojian
School of Naval Architecture and Ocean Engineering, Jiangsu University of Science and Technology

Liu, Yingyi
Research Institute for Applied Mechanics, Kyushu University

他

https://hdl.handle.net/2324/4060500

出版情報：Ocean Dynamics. 67 (9), pp.1151-1162, 2017-07-10. Springer Nature
バージョン：
権利関係：

Numerical investigation of infragravity wave amplifications during harbor oscillations influenced by variable offshore topography

Junliang Gao[1, 2, 3*], Chunyan Ji[1], Xiaojian Ma[1], Yingyi Liu[4], Oleg Gaidai[1]

1 School of Naval Architecture and Ocean Engineering, Jiangsu University of Science and Technology, Zhenjiang 212003, China

2 Jiangsu Key Laboratory of Coast Ocean Resources Development and Environment Security, Hohai University, Nanjing 210098, China

3 State Key Laboratory of Coastal and Offshore Engineering, Dalian University of Technology, Dalian 116024, China

4 Research Institute for Applied Mechanics, Kyushu University, Kasuga, Fukuoka 816-8580, Japan

Abstract:

The infragravity (IG) period oscillations inside an elongated rectangular harbor near the offshore fringing reef induced by normal-incident bichromatic short wave groups are simulated using a fully nonlinear Boussinesq model, FUNWAVE 2.0. Based on an IG wave separation procedure, this article presents a systematical investigation on how the maximum IG period component amplitude, the bound and free IG waves and their relative components inside the harbor change with respect to the plane reef-face slope and the incident short wave amplitude under the condition of the 2nd to the 5th modes. For the given harbor and the ranges of the reef-face slope and the incident short wave amplitude studied in this paper, it is shown that both the maximum IG period component amplitude and the free IG wave component amplitude inside the harbor fluctuate widely with the reef-face slope, and their changing trends with the reef-face slope are almost identical with each other; while the bound IG waves inside the harbor seem insensitive to it. Both the maximum IG period component amplitude and those of the bound and free IG standing waves inside the harbor change cubically with the incident short wave amplitude.

Key words:

Harbor Oscillations; Topography; Bound infragravity waves; Free infragravity waves; Wave

---

[*] Corresponding author. Tel.: 86-511-8444 8827, E-mail: gaojunliang880917@163.com (J. Gao).

groups; FUNWAVE 2.0 model

1. Introduction

Forcing long waves with frequencies close to those of resonant modes of the harbor can be highly amplified into inner basins causing large oscillations of the water surface (Miles, 1974; Rabinovich, 2009). Better understanding of wave trapping and amplification in bays and harbors is of vital importance to many practical applications. Several external forcings such as tsunamis originating from distance earthquake, longshore-propagating edge waves, wind and pressure fluctuations, shear flow and impact waves induced by landslides or the failure of structures near the harbor have been shown to drive these oscillations (Chen et al., 2004; De Jong and Battjes, 2004; Dong et al., 2010a; Fabrikant, 1995; Gao et al., 2017a; Gao et al., 2015, 2016c; Maa et al., 2011; Pattiaratchi and Wijeratne, 2009). However, the primary source of infragravity (IG) waves energy is the nonlinear wave-wave interaction of short wave groups propagating in shallow waters (Bowers, 1977; Mei and Agnon, 1989; Wu and Liu, 1990). González-Marco et al. (2008) investigated the effect of IG waves on port operations in Gijón harbor (Spain) and found that if IG waves are present in the wave trains, the port's inefficiency is significantly increased although the harbor offers very good protection against wind short waves. Similar situations can be also found in other ports and harbors around the world, such as the Marina di Carrara harbor in Italy (Guerrini et al., 2014), Two Rocks Marina in Australia (Thotagamuwage and Pattiaratchi, 2014a, b), Hosojima harbor in Japan (Yoshida et al., 2000), Hua-Lien harbor in Taiwan (Chen et al., 2004), Pohang New Harbor in South Korea (Kumar et al., 2014) and Port of Long Beach in California (Kofoed-Hansen et al., 2005). Therefore, to identify layouts and technical solutions that minimize the downtime of the facility, it is vital to further improve the knowledge of the IG waves inside the harbor.

The importance of bound IG waves in harbor resonance was first proved by Bowers (1977) both theoretically and experimentally. He investigated the mean free-surface oscillations in a narrow rectangular channel with constant depth and discontinuous width, and found that a train of sinusoidally modulated short wave groups incident from infinity generates not only bound IG waves but also additional free IG waves due to an imbalance between the bound IG period fluctuations in the water pressure inside and outside the harbor entrance. When the group period is close to one of the eigenperiods of the harbor, the free long waves will then be amplified. Subsequently, by using the geometric ray theory combined with parabolic approximation, Mei and Agnon (1989) investigated the IG wave oscillations induced by incident short wave groups inside a rectangular harbor with constant depth, which was exposed to the ocean without any protection. Wu and Liu (1990) adopted the multiple-scales perturbation method to extend the solution of Mei and Agnon (1989) and treated a two-dimensional rectangular harbor, which was also of constant depth, but protected by a pair of thin breakwaters. Although different harbor shapes and mathematical methods were utilized in these two papers, similar findings with those in Bowers (1977) were obtained. In the last few decades, numerous field observations and numerical simulations on the IG period waves inside harbors, such as Barbers Point harbor in Hawaii (Okihiro and Guza, 1996; Okihiro et al., 1993), Marina di Carrara harbor in Italy (Bellotti and Franco, 2011; Guerrini et al., 2014), Two Rocks Marina and Esperance harbor in Australia (Morison and Imberger, 1992; Thotagamuwage and Pattiaratchi, 2014a, b), Port of Ferrol in Spain (López and Iglesias, 2013, 2014; López et al., 2012; López et al., 2015), have confirmed those findings by revealing strong correlation between the IG period waves inside the harbor and short wave groups outside the harbor.

Recently, Dong et al. (2010b) carried out series of numerical experiments based on a fully nonlinear Boussinesq model, FUNWAVE 2.0, and adopted a wavelet-based bispectrum to investigate how the spectrum components of short wave groups take part in nonlinear wave–wave interactions during different phases of harbor resonance. The effects of short wave frequencies on the IG period components inside the harbor were also studied in that paper. Similar to Dong et al. (2010b), based on numerical simulations by the FUNWAVE 2.0 model, Dong et al. (2013) proposed a wave analysis technique to decompose the IG period components inside the harbor into bound and free IG waves, and further studied the effect of the short wavelength on the bound and the free IG waves and their relative components inside the harbor when the lowest resonant mode, which is induced by bichromatic wave groups, occurs. Subsequently, Gao et al. (2016a) expanded the studies of Dong et al. (2013) in the following two aspects. Firstly, in order to explore the similarities and differences between different modes, the resonant modes considered in Gao et al. (2016a) were extended to the lowest four modes. Secondly, the influences of not only the short wavelength but also the incident short wave amplitude on the bound and free IG waves and their relative components inside the harbor were systematically investigated. Gao et al. (2016a) found that the amplitudes of both the bound and free IG waves become more evident when the short wavelength increases, and the latter are always larger than the former due to resonant amplification, and the amplitudes of both the bound and free IG waves change quadratically with the incident short wave amplitude. For the three papers mentioned above (i.e. Dong et al. (2013); Dong et al. (2010b); Gao et al. (2016a)), the water depths inside and outside the harbor were set to a constant, and the influence of the offshore topography on harbor oscillations was not considered. More recently, in view of the fact that the offshore reefs can elevate the IG wave energy towards the nearshore and significantly enhance the IG period oscillations inside the harbor (Thotagamuwage and Pattiaratchi, 2014a), Gao et al. (2017b) further investigated the effects of the topographical variation of the offshore reefs on the bound and free IG waves and their relative components inside the harbor systematically. It was found that for the given harbor and reef ridge, the range of the reef-face slopes and the various profile shapes studied in that paper, the amplitude of the free IG waves inside the harbor increase with the increasing of the reef-face slope, while the bound IG waves seem insensitive to it.

In order to enhance the knowledge of the IG waves inside harbors involved in IG period oscillations and offshore reef topographies, this paper further investigates how the bound and free IG waves and their relative components change with respect to both the topographical variation of the offshore reefs and the incident short wave amplitude. Compared to Gao et al. (2017b), there are mainly three research developments in this paper. Firstly, in Gao et al. (2017b), only the lowest resonant mode was investigated; while in this paper, to explore the similarities and differences between different modes, we extend the resonant mode to the 2nd to the 5th modes. Secondly, the variation range of the reef-face slope studied in this paper becomes larger than that in Gao et al. (2017b). Thirdly, this paper systematically investigates the influences of the incident short wave amplitude on the maximum IG period component amplitude, the bound and free IG waves and their relative components inside the harbor. Identical to Dong et al. (2013); Dong et al. (2010b); Gao et al. (2016a); Gao et al. (2017b), all numerical experiments are performed using the FUNWAVE 2.0 model as well. For simplification, the harbor is assumed to be long and narrow, and then the free surface movement inside the harbor essentially becomes one dimensional. The still water depth inside the harbor is set to a constant, and the incident waves are bichromatic wave groups with two slightly different frequencies. The analysis technique proposed by Dong et al. (2013) is employed to decompose the IG period components inside the harbor into bound and free IG waves.

The remainder of the paper is organized as follows: Section 2 briefly introduces the numerical model and the analysis technique. Section 3 illustrates the numerical experiment setup and the experimental wave parameters. Section 4 demonstrates the simulation results, which are explained in detail. Concluding remarks based on the results are given in Section 5.

2. Numerical model and analysis technique

2.1. Numerical model

All numerical experiments in this paper are performed using the well-known and widely implemented FUNWAVE 2.0 model (Kirby et al., 2003), referring to the fully nonlinear Boussinesq wave model on curvilinear coordinates. The one-way wave maker theory proposed by Chawla and Kirby (2000) is used to generate monochromatic or random waves. Sponge layers are placed at the boundaries of the domain to effectively absorb the energy of outgoing waves with various frequencies and directions. The capability of the model to predict wave propagation and transformation from deep to shallow water has been well validated by laboratory experiments (Kirby et al., 2003).

To verify the applicability of the FUNWAVE 2.0 model to simulate harbor oscillations with strong wave nonlinearity inside the harbor, Gao et al. (2016b) used the model to reproduce the physical experiments conducted by Rogers and Mei (1978). Gao et al. (2016b) compared the numerical results of the first three super harmonics with the experimental data of Rogers and Mei (1978) for two elongated rectangular bays of different lengths. Overall agreements were observed between the measured data and the numerical results for all the three super harmonics. It was shown that the numerical model can also simulate strong nonlinear harbor oscillations accurately. Besides, to examine the ability of the FUNWAVE 2.0 model to deal with rapidly varying bathymetry over fringing reefs, Gao et al. (2017b) implemented numerical simulations of the propagation of a train of monochromatic waves over plane reef faces with different slopes. The simulated reflection coefficients were compared with the finite element method (FEM) solutions of Suh et al. (1997). Gao et al. (2017b) found that the numerical model can accurately simulate wave propagation over rapidly varying bathymetry up to the reef-face slope of S=0.8.

2.2. Analysis technique

In this article, the wave analysis technique proposed by Dong et al. (2013) is employed to decompose the IG period components inside the harbor into bound and free IG waves. This wave separation procedure starts from an analytical expression of the IG wave free surface inside the elongated rectangular harbor subjected to bichromatic short wave groups, which was first formulated by Bowers (1977). After some trigonometric manipulations, the squared amplitude of the IG period component inside the harbor can be analytically expressed as the summation of three linearly independent functions. By installing a set of wave gauges equidistantly along the center line of the harbor, the squared amplitude of the IG period component can be directly extracted from the wave elevation signals by using the discrete Fourier transform. Then, the amplitudes of the free and bound IG waves and their initial phase difference can be calculated by using the least squares method. For the detailed theory of the IG wave decomposition method, the interested reader is referred to Dong et al. (2013). Its capacity to decompose the bound and free IG waves inside the harbor under different resonant modes have been fully verified in Dong et al. (2013) and Gao et al. (2016a).

3. Numerical experimental setup

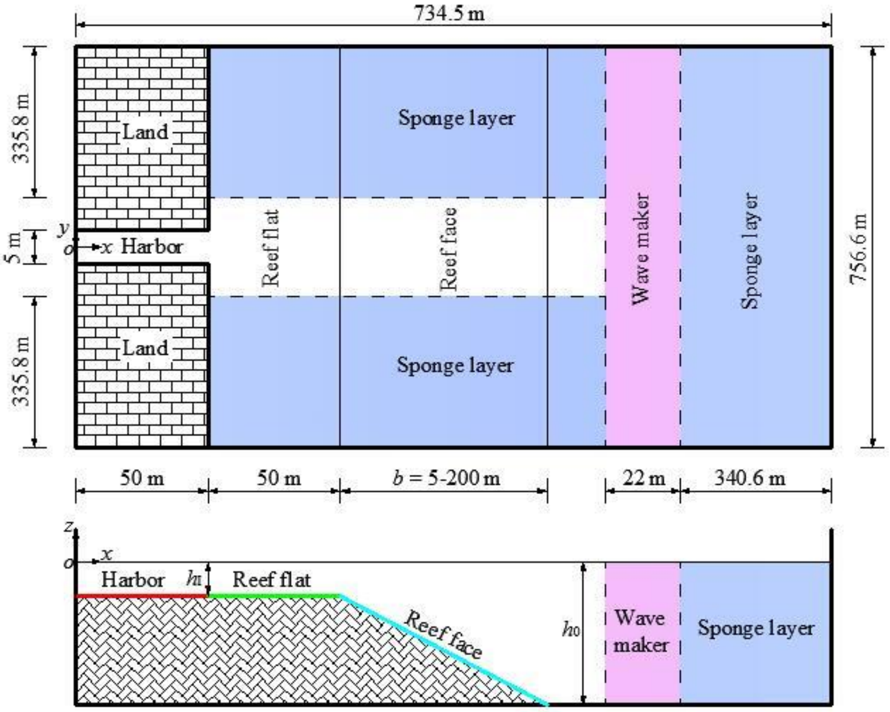

Fig. 1. Sketch of the numerical wave flume. Upper panel: top view; lower panel: longitudinal section at y=0. Since the wave tank is symmetric with respect to the x-axis, only a half-domain (i.e.

$y \geq 0$) is used for computations

Fig. 1 illustrates the numerical wave tank used in the numerical experiments. Dimensions of the numerical wave tank are 734.5 m × 756.6 m. All the boundaries are set to be fully reflective. To facilitate the comparison of the related results of higher modes with those of the lowest mode, the dimensions of the harbor and the water depths inside the harbor, over the reef flat and at the open ocean are set to be identical to those in Gao et al. (2017b). The harbor has a length of 50.0 m and a width of 5.0 m. Twenty-one wave gauges are arranged equidistantly along the center line of the harbor (not shown in the figure); the distance between adjacent gauges is 2.5 m. The gauge G_{01} is arranged near the inner end of the harbor; the gauge G_{21} is at the midpoint of the harbor entrance. The origin of the Cartesian coordinate system (o, x, y, z) is placed at the still water level with z measured upwards. The length of the reef flat located outside the harbor is set to 50.0 m. The water depth both inside the harbor and over the reef flat is a constant and equals to h_I=1.0 m, and the water depth at the open ocean is set to h_0=5.0 m. To study the influence of the reef-face slope on the IG waves inside the harbor more comprehensively, the variation range of the reef-face width is extended from 5−100 m in Gao et al. (2017b) to 5−200 m in interval of 5 m, that is, the minimum reef-face slope is extended from 0.04 in Gao et al. (2017b) to 0.02 in this paper. To absorb the energy of the radiated and reflected waves effectively, sponge layers with sufficient widths are installed at the right, bottom and upper boundaries of the wave tank. To save the computational cost, only half of the domain (i.e. $y \geq 0$) is used as the computational domain for simulations based on the geometrical symmetry with respect to the x-axis. Since the FUNWAVE 2.0 model is discretized using curvilinear grids, different grid sizes can be adopted. In the x-direction, the grid sizes Δx are all equal to 0.5 m both inside and outside the harbor except in the sponge layer at the right boundary. To reduce the large computational cost associated with the very thick sponge layer, the grid sizes Δx in the sponge layer increase gradually from 0.5 m to 10.2 m. While in the y-direction, the grid sizes Δy increase gradually from 0.5 m inside the harbor to 6.7 m outside the harbor. To obtain a good convergence rate, the Courant number $Cr = \sqrt{gh}\Delta t / \min\left(\Delta x, \Delta y\right)$ should be less than 0.5. Therefore, a time step of Δt=0.025 s is used in all simulations, and the total simulation time is 2000 s.

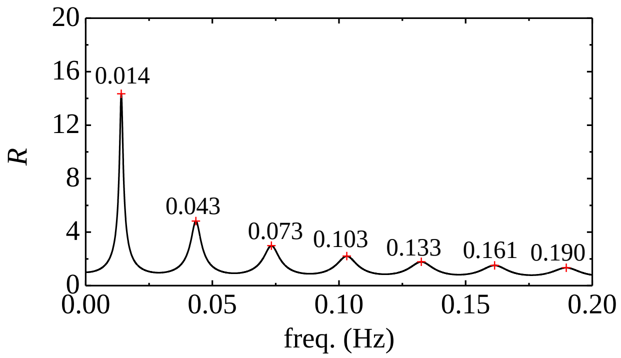

Fig. 2. Linear analytical solution of the amplification factor, R, for the harbor shown in Fig. 1, in which the numbers over the local maximum of the curve denote the corresponding eigenfrequencies.

Table 1. Incident wave parameters for all cases in Modes 2−5. For the cases with b=5 m, 100 m and 200 m, the incident short wave amplitudes, a_1=a_2, increase gradually from 0.002 m to 0.04 m in interval of 0.002 m; for the other cases, only a_1=a_2=0.04 m was simulated.

Mode	f_1 (Hz)	f_2 (Hz)	l_{Ib} (m)	l_{If} (m)	$l_{0\mathrm{b}}$ (m)	$l_{0\mathrm{f}}$ (m)	f_0 (m)	h_0/l_0
2	0.250	0.293	62.6	72.7	77.5	161.8	0.2715	0.236
3	0.250	0.323	36.2	42.7	42.4	94.2	0.2865	0.263
4	0.250	0.353	25.2	30.2	28.0	65.6	0.3015	0.291
5	0.250	0.383	19.1	23.3	20.2	49.5	0.3165	0.321

Based on the analytical solution of the linear theory for the resonance of an elongated rectangular harbor in the absence of dissipation (Mei, 1983), Fig. 2 illustrates the amplification factor of the linear long waves in the harbor shown in Fig. 1. The lowest seven eigenfrequencies of the harbor are 0.014 Hz, 0.043 Hz, 0.073 Hz, 0.103 Hz, 0.133 Hz, 0.161 Hz and 0.190 Hz, respectively. Due to the fact that the lowest resonant mode has been comprehensively investigated in Gao et al. (2017b) and the amplification factors of the 6th and higher modes are very small (close to 1.0), this paper only focuses on harbor oscillations of the 2nd to the 5th resonant modes (hereinafter, for simplicity, we use the term “Mode i” to denote the ith resonant mode). Table 1 lists the specific incident wave parameters of all the simulations. For all the four modes, the short wave frequency, f_1, is set to 0.25 Hz, and the values of the other short wave frequency, f_2, are given so that the beat frequency, $\Delta f=|f_1-f_2|$, corresponds to their respective eigenfrequencies. The symbols l_{Ib} and l_{If} in the table denote the wavelengths of the bound and free IG waves inside the harbor, respectively; l_{0b} and l_{0f} denote the wavelengths of the bound and free IG waves at the open ocean, respectively. $f_0=(f_1+f_2)/2$ denotes the average short wave frequency for each mode. $l_0 = g/(2\pi f_0^2)$ denotes the deep water wavelengths of the short waves, and g denotes the gravitational acceleration. For all the four modes in Table 1, the relative water depths of the incident short waves, h/l_0, are less than 0.321; with in this range, the FUNWAVE 2.0 model can be used to simulate the wave propagation and transformation accurately. To systematically investigate the influences of the incident short wave amplitude on the maximum IG period component amplitude, the bound and free IG waves and their relative components inside the harbor, for the cases with b=5 m, 100 m and 200 m, the incident short wave amplitudes, $a_1=a_2$, increase gradually from 0.002 m to 0.04 m in interval of 0.002 m. For the other cases, only the condition of $a_1=a_2=0.04$ m is simulated. a_1 and a_2 denote the amplitudes of the incident short wave f_1 and f_2 components, respectively.

4. Results and discussion

4.1. Time series and spectra analysis

Time series and corresponding wavelet spectra of the free surfaces at the representative wave gauge for the four cases in Modes 2−5 under the condition of under the conditions of b=200 m and $a_1=a_2=0.04$ m are illustrated in Figs. 3 and 4, respectively. The representative wave gauge refers to the one which has the maximum IG period component amplitude inside the harbor. For all the cases in Modes 2−4, the representative wave gauge corresponds to the gauge G_{01}; while for all the cases in Mode 5, it corresponds to the gauge G_{20} (this will be described in detail in the following text). It is noted that in Fig. 3, the time series of the free surfaces at the representative wave gauge are normalized by the average amplitude of the incident short waves, $a=(a_1a_2)^{1/2}$. Fig. 3 demonstrated that the free surface inside the harbor is calm at the initial period of time. For the three cases in Modes 2−4 (Fig. 3a−c), the short waves reach the position of the gauge G_{01} at approximately 80 s; while for the case in Mode 5, due to the fact that the gauge G_{20} is close to the harbor entrance, the short waves reach its position earlier, at about 60 s (Fig. 3d). Via the wavelet spectra shown in Fig. 4, the wave energy variation in both the time and frequency domains can be visually displayed. The energies of the short wave components increase from zero to their maximum levels very rapidly (about 40−60 s) and then remain relatively steady until the end of the simulations. However, more time is needed for the sub-harmonic components to attain the quasi-steady state from the initial response phase. For the four cases, it is shown that the IG period components attain the quasi-steady state at about t=350 s. In this paper, we study only the quasi-steady processes for all cases.

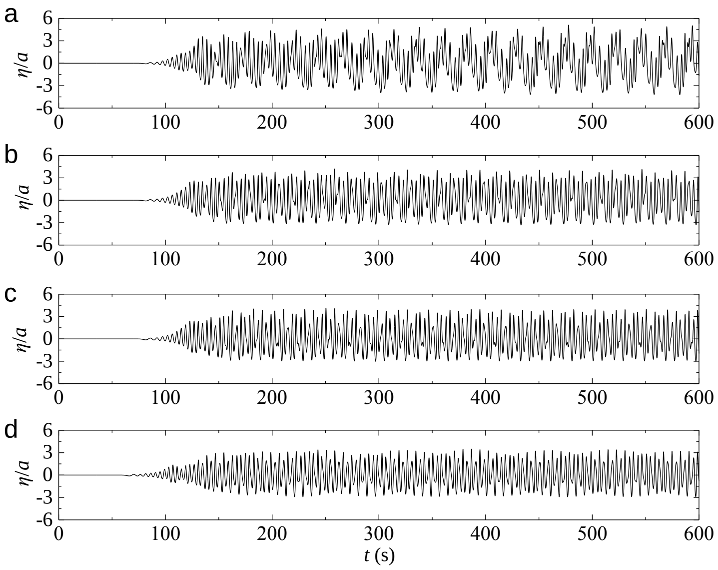

Fig. 3. Time series of the free surfaces at the representative wave gauge for the four cases in (a) Mode 2, (b) Mode 3, (c) Mode 4 and (d) Mode 5 under the conditions of a_1=a_2=0.04 m and b=200 m, in which a=$(a_1a_2)^{1/2}$. For all the cases in Modes 2−4, the representative wave gauge corresponds to the gauge G_{01}; while for all the cases in Mode 5, it corresponds to the gauge G_{20}.

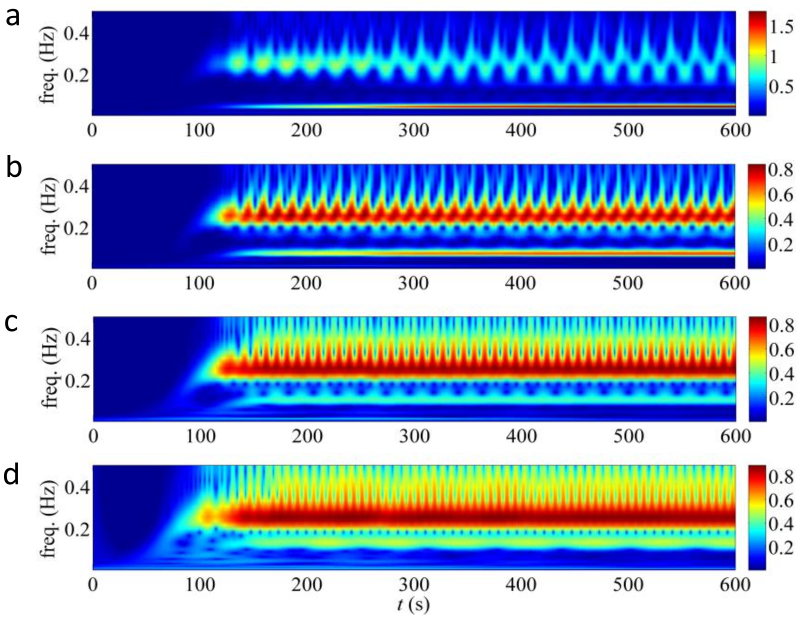

Fig. 4. Wavelet spectra at the representative wave gauges for the four cases in (a) Mode 2, (b) Mode 3, (c) Mode 4 and (d) Mode 5 under the conditions of a_1=a_2=0.04 m and b=200 m

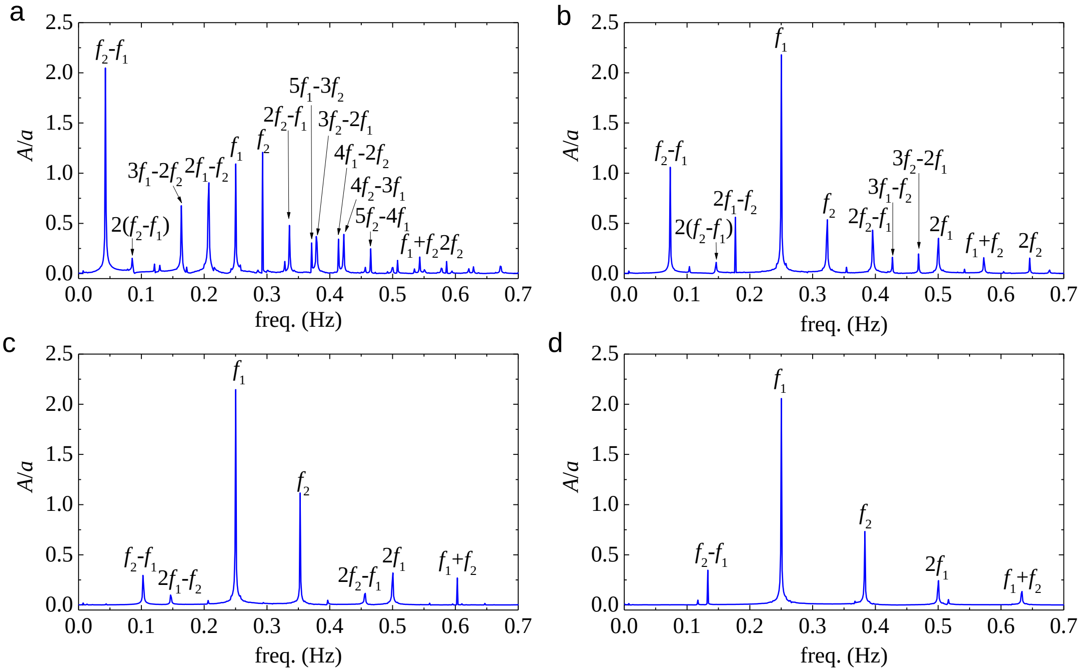

Fig. 5. Amplitude spectra at the representative wave gauge for the four cases in (a) Mode 2, (b) Mode 3, (c) Mode 4 and (d) Mode 5 under the conditions of a_1=a_2=0.04 m and b=200 m

The spectral analysis of the simulated free surface elevations is carried out with the time segment of 361.6–2000.0 s (time interval is 0.025 s, hence the total number of temporal points=2^{16}). Fig. 5 illustrated the amplitude spectra at the representative wave gauge for the four cases shown in Figs. 3 and 4. For the case in Mode 2 (Fig. 5a), the nonlinear energy transfer between the short wave f_1 and f_2 components and the high-order wave components are intense and complicated. Besides the short wave f_1 and f_2 components, the amplitudes of the second- and higher-order wave components (f_2-f_1, $2f_2-2f_1$, $3f_1-2f_2$, $2f_1-f_2$, $2f_2-f_1$, $5f_1-3f_2$, $3f_2-2f_1$, $4f_1-2f_2$, $4f_2-3f_1$, $5f_2-4f_1$, f_1+f_2, $2f_2$) are also remarkable. For the sub-harmonic wave f_2-f_1 component, its amplitude is considerably larger than those of both the short wave f_1 and f_2 components. For the case in Mode 3 (Fig. 5b), although the nonlinear energy transfer between different wave components is weaker than that shown in Fig. 5a, besides the short wave f_1 and f_2 components, the second- and higher-order wave components (f_2-f_1, $2f_2-2f_1$, $2f_1-f_2$, $2f_2-f_1$, $3f_1-f_2$, $3f_2-2f_1$, $2f_1$, f_1+f_2, $2f_2$) can still be clearly observed. Although the amplitude of the sub-harmonic wave f_2-f_1 component is less than that of short wave f_1 component, it still exceeds that of the short wave f_2 component. For the two cases in Modes 4 and 5 (Fig. 5c and d), the nonlinear energy transfer is much weaker than that in the cases in Mode 2 and 3. For the high-order wave components, only the components $2f_1$, f_1+f_2, f_2-f_1 are marked.

4.2. Effects of the reef-face slope on IG waves

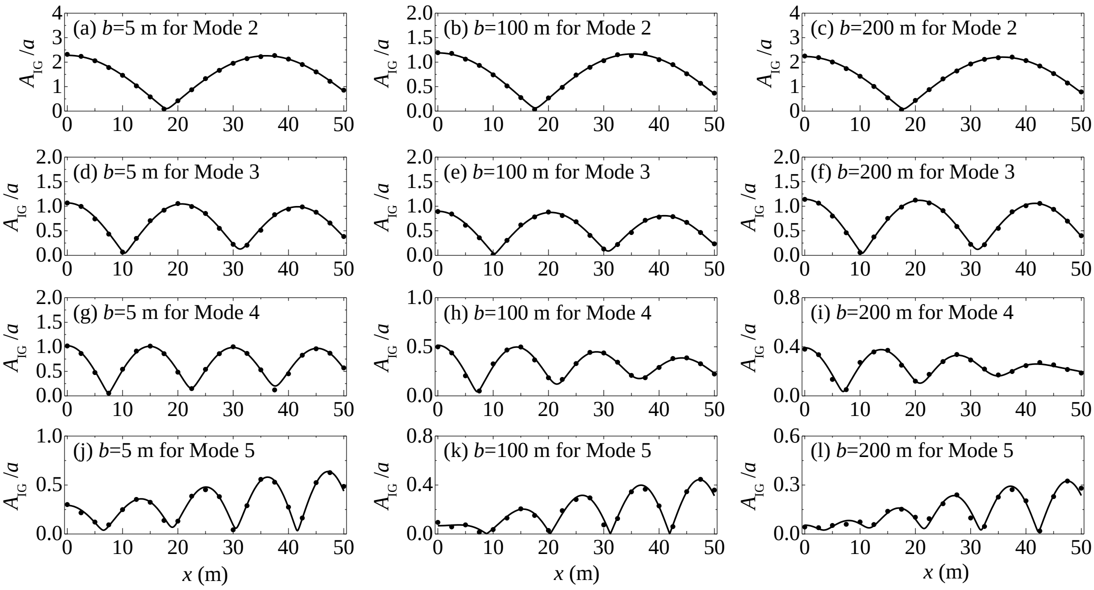

Fig. 6. Amplitudes of the IG period components (dots) at all wave gauges and their envelopes (solid lines) obtained using the separation procedure for cases with different resonant modes and different reef-face widths under the condition of $a_1=a_2=0.04$ m

Using the IG wave separation procedure described in Section 2.2, the bound and free IG standing waves inside the harbor are decomposed in all the numerical experiments. Fig. 6 illustrates the amplitudes of the IG period components for all wave gauges and their fitted envelopes obtained using the separation procedure for cases with different resonant modes and different reef-face widths under the condition of $a_1=a_2=0.04$ m (where A_{IG} denotes the IG period component amplitude). It is shown that the IG period component amplitudes at all wave gauges are very close to their fitted envelopes in all the twelve cases, which indicates that the separating amplitudes of the bound and free IG wave components obtained using the IG wave analysis technique are accurate and reliable. Meanwhile, it can be observed that for all the nine cases in Modes 2−4 (Fig. 6a−i), the maximum IG period component amplitude inside the harbor always appears at the backwall of the harbor where the gauge G_{01} is placed. The phenomenon is accordance with the findings in the previous relevant researches (i.e. Dong et al. (2013); Gao et al. (2016a); Gao et al. (2017b)) in which the lowest mode or the lowest four modes are investigated.

However, for all the three cases in Mode 5 (Fig. 6j−l), the maximum IG period component amplitude inside the harbor no longer appears at the backwall of the harbor, but appear at the position of the gauge G_{20}. To further examine the phenomenon, Fig. 7 presents the comparison of the amplitude spectra at the gauges G_{01} and G_{20} in the three cases shown in Fig. 6j−l. For all the three cases in Mode 5, the amplitudes of the short wave f_1 components at the two gauges are almost identical, and the amplitude of the short wave f_2 component at the gauge G_{01} is always obviously larger than that at the gauge G_{20}. However, the IG period component amplitude corresponding to the beat frequency f_2−f_1 at the gauge G_{01} is always less than that at the gauge G_{20}. It further proves that the maximum IG period component amplitude inside the harbor doesn't always appear at the backwall, and for certain high modes, its position may shift to a certain place near the harbor entrance.

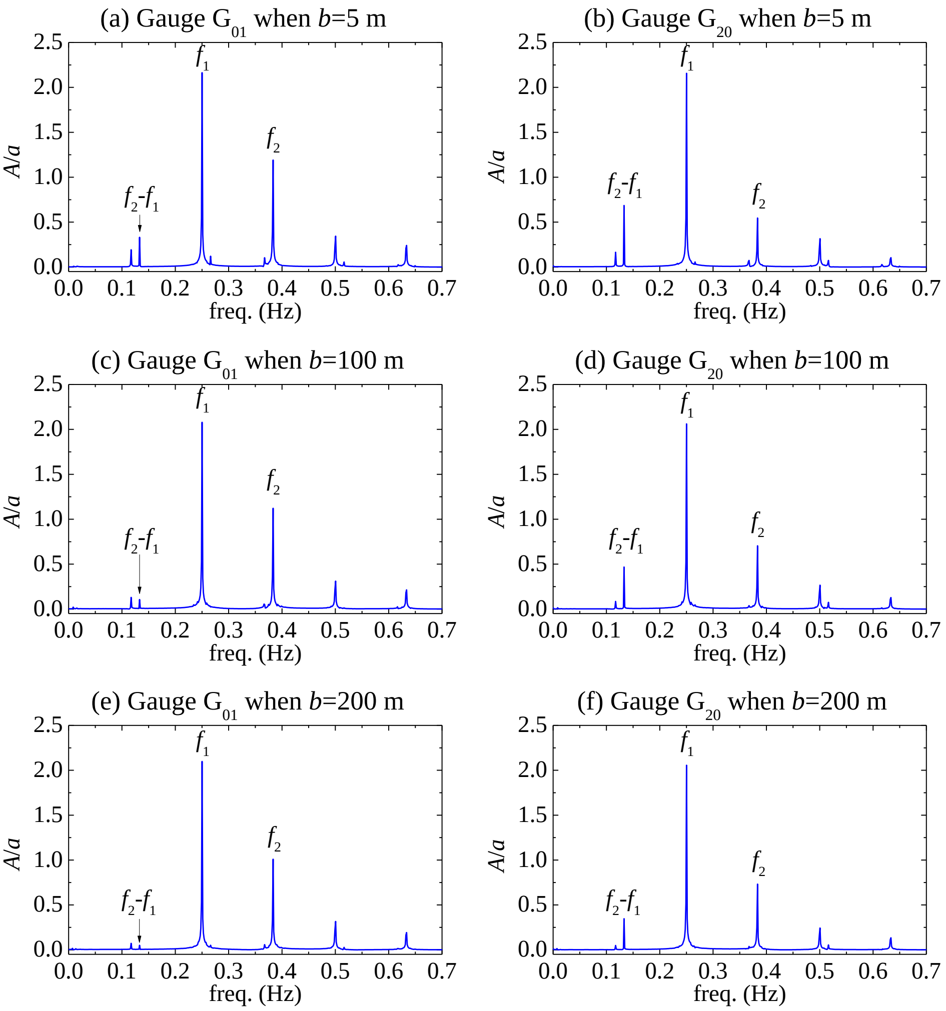

Fig. 7. Comparison of the amplitude spectra at the gauges G_{01} and G_{20} for the three cases in Mode

5 with b=5 m, 100 m and 200 m under the condition of a_1=a_2=0.04 m.

Table 2. The separation results of the bound and free IG waves for the twelve cases shown in Fig. 6. A_m in this table denotes the maximum IG period component amplitude inside the harbor, which corresponds to the IG wave amplitudes at the gauge G_{01} for Modes 2-4 and those at the gauge G_{20} for Mode 5.

Case	Results				
	A_m (m)	ζ_b (m)	ζ_f (m)	$\lvert\alpha_b-\alpha_f\rvert$ (°)	ζ_b/ζ_f (%)
(a)	0.0926	0.0180	0.0865	80.87	20.79
(b)	0.0477	0.0139	0.0402	66.42	34.60
(c)	0.0899	0.0178	0.0820	71.90	21.75
(d)	0.0426	0.0094	0.0366	55.51	25.78
(e)	0.0355	0.0094	0.0278	35.95	34.03
(f)	0.0456	0.0095	0.0391	50.93	24.35
(g)	0.0407	0.0081	0.0389	82.50	20.83
(h)	0.0199	0.0081	0.0160	65.99	50.58
(i)	0.0152	0.0083	0.0103	65.54	80.45
(j)	0.0250	0.0077	0.0185	159.0	41.57
(k)	0.0172	0.0074	0.0101	175.7	72.67
(l)	0.0130	0.0073	0.0060	165.4	123.0

To reasonably explain the difference of the position where the maximum IG period component amplitude inside the harbor appears between Modes 2-4 and Mode 5, the separation results of the twelve cases shown in Fig. 6 are listed in Table 2. It is noted that in this table, A_m denotes the maximum IG period component amplitude inside the harbor, which corresponds to the IG wave amplitudes at the gauge G_{01} for Modes 2−4 and those at the gauge G_{20} for Mode 5. ζ_b and ζ_f denote the amplitudes of the bound and free IG standing waves, respectively, and α_b and α_f denote their respective initial phases. It can be found that for all the three cases in Mode 5 (i.e. cases j−l), the initial phase differences of the bound and free IG standing waves inside the harbor, $|\alpha_b-\alpha_f|$, approach 180°. It means that the bound and free IG standing waves inside the harbor are almost anti-phase. According to the formulation of Bowers (1977), the IG period component free-surface inside the harbor can be analytically expressed as the linear superposition of the bound and free IG standing waves:

$$\eta = \zeta_\mathrm{b}\cos[(2\pi\Delta f)t - \alpha_\mathrm{b}]\cos(\Delta k x) + \zeta_\mathrm{f}\cos[(2\pi\Delta f)t - \alpha_\mathrm{f}]\cos(\kappa x), \tag{1}$$

where

$$\Delta f = |f_1 - f_2|, \tag{2}$$

$$\Delta k = |k_1 - k_2|, \tag{3}$$

and k_1 and k_2 denote the wavenumbers of the short wave f_1 and f_2 components, respectively. (f_1, k_1) and (f_2, k_2) satisfy the linear dispersion relation:

$$(2\pi f_i)^2 = g k_i \tanh(k_i h_\mathrm{I}) \quad (i = 1, 2). \tag{4}$$

Δk and κ denote the wavenumber of the bound and free IG waves, respectively, and (κ, Δf) also satisfy the linear dispersion relation. When the bound and free IG waves inside the harbor approach anti-phase, both the bound and free IG wave components cancel each other out near the backwall of the harbor, which leads to the phenomenon that the maximum IG period component amplitude for the three cases in Mode 5 does not appear at the backwall, but appear at a place near harbor entrance. On the contrary, for the nine cases in Modes 2−4 (i.e. cases a−i), the initial phase differences of the bound and free IG waves inside the harbor, $|\alpha_\mathrm{b} - \alpha_\mathrm{f}|$, are all less than 90°. The bound and free IG wave components do not cancel each other out near the backwall of the harbor. Hence, the maximum IG period component amplitude always appears at the backwall for these cases.

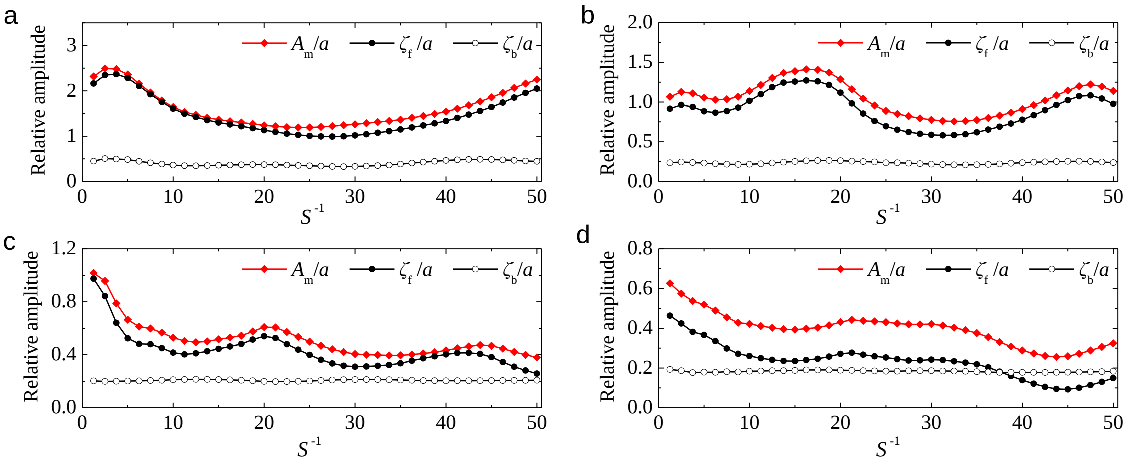

Fig. 8. Variations of the maximum IG period component amplitude and the corresponding separating amplitudes of the bound and free IG waves inside the harbor with respect to the slope

coefficient, S^{-1}, for all cases in (a) Mode 2, (b) Mode 3, (c) Mode 4 and (d) Mode 5 under the condition of a_1=a_2=0.04 m.

For the reef faces with different plane slopes, the variations of the maximum IG period component amplitude and the corresponding separating amplitudes of the bound and free IG waves inside the harbor with respect to the slope coefficient, S^{-1}, for all cases in Modes 2−5 under the condition of a_1=a_2=0.04 m are presented in Fig. 8. Three phenomena can be visually observed in the figure. Firstly, for all the four resonant modes studied in this paper, the influence of the reef-face slope on the bound IG wave component inside the harbor seems negligible, which is consistent with the findings for the lowest mode in Gao et al. (2017b). Secondly, both the maximum IG period component amplitude and the free IG wave component amplitude inside the harbor fluctuate widely with the reef-face slope. Besides, the two fluctuating curves are almost paralleled with each other. Thirdly, for the cases in Modes 2−4, the amplitudes of the free IG waves are always larger than those of the bound IG waves inside the harbor, which is due to that the free IG waves in the three modes have relatively large linear amplification factors (refer to Fig. 2) and are significantly amplified inside the harbor. While for the cases in Mode 5, when the slope coefficient $S^{-1} \leq 37.5$ (equivalently, $S \geq 0.0267$), the amplitudes of the free IG waves are always larger than those of the bound IG waves inside the harbor. With the increase of the slope coefficient, the former becomes less than the latter. This can be explained qualitatively as follows: although the free IG wave component corresponds to Mode 5, its linear amplification factor is relatively small (only about 1.79). The amplification effect of the harbor on the free IG wave component inside the harbor is relatively limited. Hence, the relative component of the bound and free IG waves inside the harbor is more sensitive to the reef-face slope. To illustrate this point more visually, Fig. 9 shows the variations of the amplitude ratios, ζ_b/ζ_f , with respect to the slope coefficient, S^{-1}, for all cases in Modes 2−5 under the condition of a_1=a_2=0.04 m. It is observed that for Modes 2 and 3, the values of ζ_b/ζ_f fluctuate only in the ranges of 21.7−34.6% and 19.5−37.5%, respectively. For Mode 4 in which the linear amplification factor of the free IG waves is less than those in Modes 2 and 3, the values of ζ_b/ζ_f have a larger variation range of 20.8−80.5%. Compared to Mode 4, the linear amplification factor of the free IG waves in Mode 5 becomes smaller, and the variation range of ζ_b/ζ_f widens further from 41.6% to 192.8%.

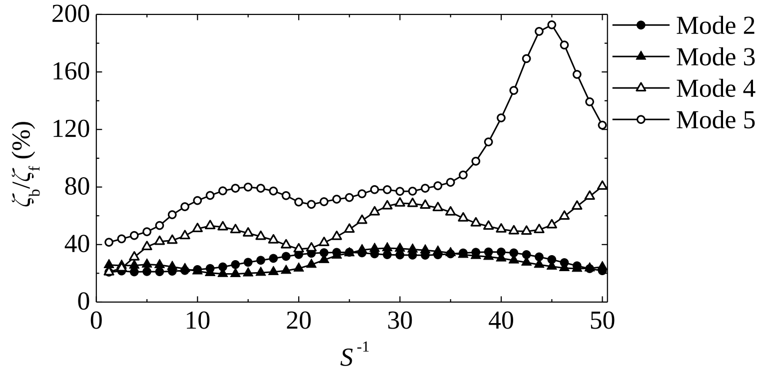

Fig. 9. The amplitude ratios, ζ_b/ζ_f , for all cases in Modes 2−5 under the condition of a_1=a_2=0.04 m.

Fig. 10 presents the initial phase differences of the bound and free IG waves, $|\alpha_b-\alpha_f|$, for all cases in Modes 2−5 under the condition of a_1=a_2=0.04 m. It is shown that for all the cases in Modes 2−4, the values of $|\alpha_b-\alpha_f|$ are always less than 100°, which coincides with the phenomenon that the maximum IG period component amplitude inside the harbor always appears at the backwall of the harbor. While for all the cases in Mode 5, the values of $|\alpha_b-\alpha_f|$ fluctuate around 180°, which leads to the countervailing effects between the bound and free IG standing waves at the backwall of the harbor and causes the phenomenon that the maximum IG period component amplitude appears at a certain place near the harbor entrance.

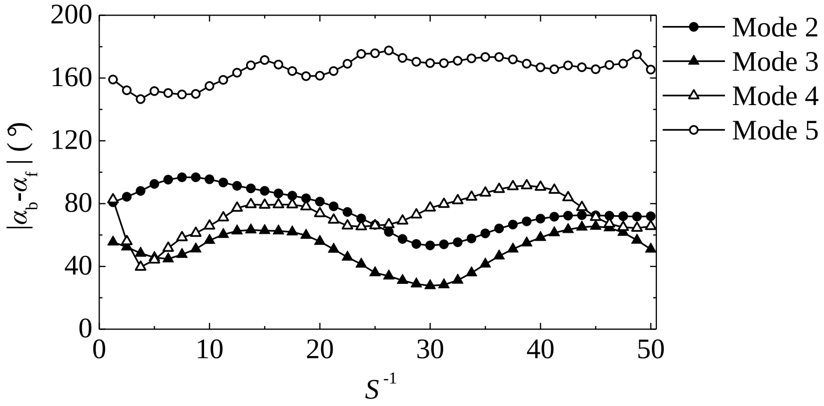

Fig. 10. The initial phase differences of the bound and free IG waves, $|\alpha_b-\alpha_f|$, for all cases in Modes 2−5 under the condition of a_1=a_2=0.04 m.

4.3. Effects of the incident wave amplitude on IG waves

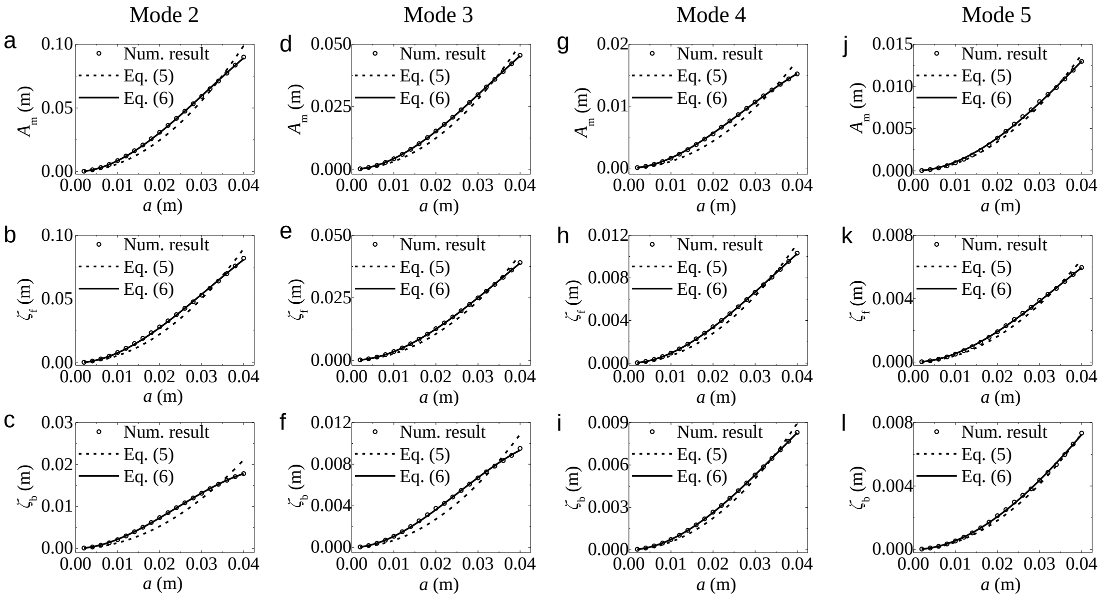

Fig. 11. Variation of the maximum IG period component amplitude, A_m, and the separating bound and free IG wave amplitudes, ζ_b and ζ_f, with respect to the average amplitude of the incident short waves, a, under the condition of b=200 m. (a)−(c), (d)−(f), (g)−(i) and (j)−(l) correspond to the cases in Modes 2−5, respectively. The open circles denote the maximum IG period component amplitude and the separating bound and free IG wave amplitudes; the dashed and solid curves denote the corresponding fitted amplitudes by Eqs. (5) and (6), respectively.

To investigate systematically the effects of the incident wave amplitude on the IG waves inside the harbor, for the cases in Modes 2−5 with the reef-face width b=5 m, 100 m and 200 m, the incident short wave amplitudes, a_1=a_2, increase gradually from 0.002 m to 0.04 m in interval of 0.002 m. Fig. 11 illustrates the variation the maximum IG period component amplitude, A_m, and the separating bound and free IG wave amplitudes, ζ_b and ζ_f, with respect to the average amplitude of the incident short waves, a, under the condition of b=200 m. By investigating the IG period oscillations inside an elongated harbor, Gao et al. (2016a) found that the amplitudes of both the bound and free IG waves change quadratically with the amplitudes of the incident short waves. It is noted that the water depth inside and outside the harbor in Gao et al. (2016a) was set to a constant. From this figure, it can be observed intuitively that the maximum IG period component amplitude, A_m, and the separating bound and free IG wave amplitudes, ζ_b and ζ_f, also seem to change quadratically with the incident short wave amplitude, that is,

$$\psi = C \cdot a^2, \tag{5}$$

in which ψ denotes A_{m}, ζ_{b} or ζ_{f}, and C is an unknown coefficient which can be determined by using the least squares method. The fitted results by Eq. (5) are also shown in Fig. 11 as dashed curves. It is found that for some cases, the quadratic expression, Eq. (5), can only roughly describe the changing trends of A_{m}, ζ_{b} and ζ_{f}, and its prediction accuracy is not very high. Take the case in Mode 2 (Fig. 11a−c) for example. For all the parameters of A_{m}, ζ_{b} and ζ_{f}, Eq. (5) underestimates their values obviously when $a \leq 0.35$ m; while with the further increase of a, Eq. (5) gradually becomes to significantly overestimate their values.

Table 3. Values of the parameters C, D_i (i=1 and 2), the coefficient of determination R^2 and the root mean square errors *RMSE* corresponding to the fitted curves shown in Fig. 11.

Case	$\psi=C\cdot a^2$			$\psi=D_1\cdot a^2+D_2\cdot a^3$			
	C	R^2	*RMSE*	D_1	D_2	R^2	*RMSE*
(a)	61.83	0.9751	4.64×10^{-3}	97.07	-1032	0.9999	3.21×10^{-4}
(b)	55.91	0.9761	4.10×10^{-3}	86.9	-908	0.9996	5.29×10^{-4}
(c)	13.2	0.9322	1.58×10^{-3}	25.23	-352.4	0.9999	5.56×10^{-5}
(d)	31.16	0.9793	2.15×10^{-3}	47.51	-479	1	9.04×10^{-5}
(e)	26.36	0.9845	1.58×10^{-3}	38.38	-352.3	0.9999	9.26×10^{-5}
(f)	6.793	0.9463	7.28×10^{-4}	12.31	-161.7	0.9996	6.43×10^{-5}
(g)	10.86	0.9603	1.02×10^{-3}	18.6	-226.7	0.9999	4.39×10^{-5}
(h)	7.001	0.982	4.51×10^{-4}	10.43	-100.3	0.9999	2.74×10^{-5}
(i)	5.594	0.9862	3.18×10^{-4}	8.013	-70.88	1	9.52×10^{-6}
(j)	8.613	0.9919	3.84×10^{-4}	11.44	-82.83	0.9995	9.96×10^{-5}
(k)	4.048	0.984	2.48×10^{-4}	5.921	-54.89	0.9998	3.02×10^{-5}
(l)	4.571	0.9975	1.19×10^{-4}	5.83	-32.56	0.9996	4.79×10^{-5}

To further improve the prediction accuracy of A_{m}, ζ_{b} and ζ_{f} inside the harbor, in this paper, by adding an additional cubic correction term, Eq. (5) proposed by Gao et al. (2016a) is modified to

$$\psi=D_1\cdot a^2+D_2\cdot a^3, \tag{6}$$

in which D_1 and D_2 are unknown coefficients which can also be determined by using the least squares method. The fitted results by Eq. (6) are also presented in Fig. 11 as solid curves. It can be found that in the range of the incident short wave amplitude studied in this paper, compared to Eq. (5), Eq. (6) shows a much better correlation with the numerical data. Table 3 presents the values of the parameters C, D_i (i=1 and 2), the coefficient of determination R^2 and the root mean square errors *RMSE* corresponding to the fitted curves shown in Fig. 11. The quantitative result shows that the fitted curves of Eq. (6) in all the cases have larger values of R^2 compared with the corresponding fitted results of Eq. (5). Besides, the values of *RMSE* obtained by the former are only $O(10^{-1}–10^{-2})$ times those obtained by the latter. This coincides with the phenomena shown in Fig. 11. It should be stressed here that the fitted results of Eqs. (5) and (6) with the numerical data for the cases with b=5 m and 100 m reveal the same phenomena as those shown in Fig. 11 and Table 3, and due to the limitation of space, their specific fitted results are not presented in this article. Therefore, in the range of the incident short wave amplitude studied in this paper, Eq. (6) with the terms of a^2 and a^3 seems to be able to accurately describe the amplification of the IG waves inside the harbor.

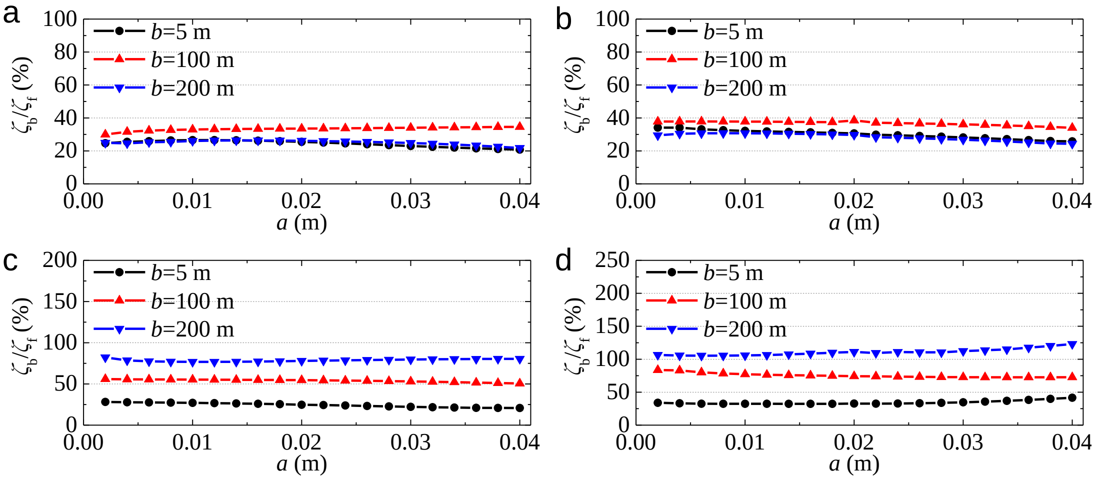

Fig. 12. Variation of the amplitude ratios, ζ_b/ζ_f, with respect to the average amplitude of the incident short waves, a, in (a) Mode 2, (b) Mode 3, (c) Mode 4 and (d) Mode 5

Fig. 12 presents the variation of the amplitude ratios, ζ_b/ζ_f, with respect to the average amplitude of the incident short waves, a. It can be found intuitively that when the 2nd to the 5th resonant modes occur inside the harbor, the amplitude ratio in each case are only slightly affected by the incident short wave amplitude regardless of whether the reef-face width is large or not. It coincides with the finding of Gao et al. (2016a) in which the water depth inside and outside the harbor was a constant.

5. Conclusions

The IG period oscillations under the 2nd to the 5th resonant modes inside an elongated rectangular harbor near the offshore fringing reef excited by normal-incident bichromatic short wave groups are simulated using the FUNWAVE 2.0 model. The IG wave separation procedure proposed by Dong et al. (2013) is used to decompose the IG period components inside the harbor into bound and free IG waves. Effects of the plane reef-face slope and the incident short wave amplitude on the maximum IG period component amplitude, the bound and free IG waves and their relative components inside the harbor are investigated systematically. The results of this study will improve the understanding of IG waves inside harbors involved in IG period oscillations and offshore reef topographies.

The following conclusions can be drawn from the results of the present study:

1. For the 2nd to the 4th mode, the maximum IG period component amplitude inside the harbor always appears at the backwall of the harbor; while for the 5th mode, due to that the initial phase difference of the bound and free IG waves fluctuates around 180°, the IG period component near the backwall is obviously inhibited, and the position of the maximum IG period component amplitude shifts to a certain place near the harbor entrance.
2. For all the resonant modes considered in this paper, both the maximum IG period component amplitude and the free IG wave component amplitude inside the harbor fluctuate widely with the reef-face slope, and their changing trends with the reef-face slope are almost identical with each other. On the contrary, the influence of the reef-face slope on the bound IG wave component inside the harbor seems negligible. The relative component of the bound and free IG waves inside the harbor tends to become more sensitive to the reef-face slope with the increase of the resonant mode.
3. For the incident short wave amplitude range studied in this paper, Eq. (6) with the terms of a^2 and a^3 seems to accurately describe the amplifications of both the maximum IG period component amplitude and those of the bound and free IG standing waves inside the harbor. Besides, the amplitude ratios of the bound and free IG waves, ζ_b/ζ_f, are only slightly affected by the incident short wave amplitude.

Finally, we reaffirm here that these conclusions are only valid for the given harbor and the ranges of the reef-face slope and the incident short wave amplitude studied in this paper. The wave breaking and the associated wave set-up/set-down over fringing reefs may markedly change the distribution and strength of the IG period component inside the harbor. These processes are not considered in the current study.

Acknowledgments

This work was financially supported by the National Natural Science Foundation of China (Grant nos. 51609108, 51309124 and 51679113), the Natural Science Foundation of the Jiangsu Higher Education Institutions of China (Grant no. 16KJB570004), the State Key Laboratory of Coastal and Offshore Engineering at Dalian University of Technology (Grant no. LP1602), the Jiangsu Key Laboratory of Coast Ocean Resources Development and Environment Security at Hohai University (Grant no. JSCE201508) and the Jiangsu Key Laboratory of Advanced Design and Manufacturing Technology for Ship at Jiangsu University of Science and Technology (Grant no. CJ1504).

References

Bellotti, E.C., Franco, L., 2011. Measurement of long waves at the harbor of Marina di Carrara, Italy. Ocean Dynamics 61 (12), 2051-2059.

Bowers, E.C., 1977. Harbour resonance due to set-down beneath wave groups. Journal of Fluid Mechanics 79, 71-92.

Chawla, A., Kirby, J.T., 2000. A source function method for generation of waves on currents in Boussinesq models. Applied Ocean Research 22 (2), 75-83.

Chen, G.-Y., Chien, C.-C., Su, C.-H., Tseng, H.-M., 2004. Resonance induced by edge waves in Hua-Lien Harbor. Journal of Oceanography 60, 1035-1043.

De Jong, M.P.C., Battjes, J.A., 2004. Seiche characteristics of Rotterdam Harbour. Coastal Engineering 51 (5-6), 373-386.

Dong, G., Gao, J., Ma, X., Wang, G., Ma, Y., 2013. Numerical study of low-frequency waves during harbor resonance. Ocean Engineering 68, 38-46.

Dong, G., Wang, G., Ma, X., Ma, Y., 2010a. Harbor resonance induced by subaerial landslide-generated impact waves. Ocean Engineering 37 (10), 927-934.

Dong, G., Wang, G., Ma, X., Ma, Y., 2010b. Numerical study of transient nonlinear harbor resonance. Science China-Technological Sciences 53, 558-565.

Fabrikant, A.L., 1995. Harbor oscillations generated by shear flow. Journal of Fluid Mechanics 282, 203-217.

Gao, J., Ji, C., Gaidai, O., Liu, Y., 2016a. Numerical study of infragravity waves amplification during harbor resonance. Ocean Engineering 116, 90-100.

Gao, J., Ji, C., Gaidai, O., Liu, Y., Ma, X., 2017a. Numerical investigation of transient harbor oscillations induced by N-waves. Coastal Engineering, http://dx.doi.org/10.1016/j.coastaleng.2017.03.004. (Available online)

Gao, J., Ji, C., Liu, Y., Gaidai, O., Ma, X., Liu, Z., 2016b. Numerical study on transient harbor oscillations induced by solitary waves. Ocean Engineering 126, 467-480.

Gao, J., Ji, C., Liu, Y., Ma, X., Gaidai, O., 2017b. Influence of offshore topography on the amplification of infragravity oscillations within a harbor. Applied Ocean Research 65, 129-141.

Gao, J., Ma, X., Dong, G., Wang, G., Ma, Y., 2015. Improvements on the normal mode decomposition method used in harbor resonance. Proceedings of the Institution of Mechanical Engineers, Part M: Journal of Engineering for the Maritime Environment 229 (4), 397-410.

Gao, J., Ma, X., Dong, G., Wang, G., Ma, Y., 2016c. Numerical study of transient harbor resonance induced by solitary waves. Proceedings of the Institution of Mechanical Engineers, Part M: Journal of Engineering for the Maritime Environment 230 (1), 163–176.

González-Marco, D., Sierra, J.P., Ybarra, O.F.d., Sánchez-Arcilla, A., 2008. Implications of long waves in harbor management: The Gijón port case study. Ocean & Coastal Management 51 (2), 180-201.

Guerrini, M., Bellotti, G., Fan, Y., Franco, L., 2014. Numerical modelling of long waves amplification at Marina di Carrara Harbour. Applied Ocean Research 48, 322-330.

Kirby, J.T., Long, W., Shi, F., 2003. Funwave 2.0 Fully Nonlinear Boussinesq Wave Model On Curvilinear Coordinates. Report No. CACR-02-xx. Center for Applied Coastal Research, Dept. of Civil & Environmental Engineering, University of Delaware, Newark, Delaware.

Kofoed-Hansen, H., Kerper, D.R., Sørensen, O.R., Kirkegaard, J., 2005. Simulation of long wave agitation in ports and harbours using a time-domain Boussinesq model. Proceedings of the Fifth International Symposium on Ocean Wave Measurement and Analysis (WAVES), Madrid, Spain.

Kumar, P., Zhang, H., Kim, K.I., 2014. Spectral Density Analysis for Wave Characteristics in Pohang New Harbor. Pure and Applied Geophysics 171, 1169-1185.

López, M., Iglesias, G., 2013. Artificial intelligence for estimating infragravity energy in a harbor. Ocean Engineering 57, 56-63.

López, M., Iglesias, G., 2014. Long wave effects on a vessel at berth. Applied Ocean Research 47, 63-72.

López, M., Iglesias, G., Kobayashi, N., 2012. Long period oscillations and tidal level in the Port of Ferrol. Applied Ocean Research 38, 126-134.

López, M., López, I., Iglesias, G., 2015. Hindcasting Long Waves in a Port: An ANN Approach. Coastal Engineering Journal 57 (4), 1550019-1-20.

Maa, J.P.-Y., Tsai, C.-H., Juang, W.-J., Tseng, H.-M., 2011. A preliminary study on Typhoon Tim induced resonance at Hualien Harbor, Taiwan. Ocean Dynamics 61, 411-423.

Mei, C.C., 1983. The Applied Dynamics of Ocean Surface Waves. Wiley, New York.

Mei, C.C., Agnon, Y., 1989. Long-period oscillations in a harbour induced by incident short waves. Journal of Fluid Mechanics 208, 595-608.

Miles, J.W., 1974. Harbor seiching. Annual Review of Fluid Mechanics 6, 17-33.

Morison, M.L., Imberger, J., 1992. Water-Level Oscillations in Esperance Harbour. Journal of Waterway, Port, Coastal, and Ocean Engineering 118 (4), 352-367.

Okihiro, M., Guza, R.T., 1996. Observations of seiche forcing and amplification in three small harbors. Journal of Waterway, Port, Coastal and Ocean Engineering 122 (5), 232-238.

Okihiro, M., Guza, R.T., Seymour, R.J., 1993. Excitation of Seiche Observed in a Small Harbor. Journal of Geophysical Research 98 (C10), 18201-18211.

Pattiaratchi, C.B., Wijeratne, E.M.S., 2009. Tide gauge observations of 2004-2007 Indian Ocean tsunamis from Sri Lanka and Western Australia. Pure and Applied Geophysics 166 (1), 233-258.

Rabinovich, A.B., 2009. Seiches and harbor oscillations, in: Kim, Y. (Ed.), Handbook of Coastal and Ocean Engineering. World Scientific Publishing, Singapore, pp. 193-236.

Rogers, S.R., Mei, C.C., 1978. Nonlinear resonant excitation of a long and narrow bay. Journal of Fluid Mechanics 88 (1), 161-180.

Suh, K.D., Lee, C., Park, W.S., 1997. Time-dependent equations for wave propagation on rapidly varying topography. Coastal Engineering 32 (2-3), 91-117.

Thotagamuwage, D.T., Pattiaratchi, C.B., 2014a. Influence of offshore topography on infragravity period oscillations in Two Rocks Marina, Western Australia. Coastal Engineering 91, 220-230.

Thotagamuwage, D.T., Pattiaratchi, C.B., 2014b. Observations of infragravity period oscillations in a small marina. Ocean Engineering 88, 435-445.

Wu, J.K., Liu, P.L.-F., 1990. Harbour excitations by incident wave groups. Journal of Fluid Mechanics 217, 595-613.

Yoshida, A., Murakami, K., Uchida, M., Irie, I., 2000. Long period water surface oscillations and ship motions in Hosojima Harbor. Proceedings of the 27th International Conference on Coastal Engineering American Society of Civil Engineers, Sydney, Australia, pp. 3655-3668.